UNIVERSITY OF HELSINKI REPORT SERIES IN ASTRONOMY

No. 27

Asteroid and meteorite compositional studies by modeling light scattering

Julia Martikainen

Academic dissertation

Department of Physics
Faculty of Science
University of Helsinki
Helsinki, Finland

Doctoral dissertation, to be presented for public discussion with the permission of the Faculty of Science of the University of Helsinki, in Auditorium E204, Physicum building on the 11th of February, 2021 at 15:15 o'clock.

Helsinki 2021

ISSN 1799-3024 (print version)
ISBN 978-951-51-6964-8 (print version)
Helsinki 2021
Helsinki University Print (Unigrafia)

ISSN 1799-3032 (pdf version)
ISBN 978-951-51-6965-5 (pdf version)
ISSN-L 1799-3024
http://ethesis.helsinki.fi/
Helsinki 2021
Electronic Publications @ University of Helsinki
(Helsingin yliopiston verkkojulkaisut)

Julia Martikainen: **Asteroid and meteorite compositional studies by modeling light scattering**, University of Helsinki, 2021, 40 p. + appendices, University of Helsinki Report Series in Astronomy, No. 27, ISSN 1799-3024 (print version), ISBN 978-951-51-6964-8 (print version), ISSN 1799-3032 (pdf version), ISBN 978-951-51-6965-5 (pdf version), ISSN-L 1799-3024

Abstract

Physical characterization of asteroid surfaces by studying the scattered light is challenging as the light-scattering processes are affected by the particle sizes, shapes, and materials, which in most cases are unknown. When interpreting remote-sensing observations, it is important to choose the correct methods for realistic analyses. In the past decades, several extensive studies have been carried out to understand asteroid surfaces, however, none of the previously used models are able to interpret spectroscopy, photometry, and polarimetry at the same time with sufficient precision. In the thesis, light-scattering methods were developed and utilized together with laboratory measurements to characterize asteroid regoliths and meteorite surfaces.

The light-scattering methods presented in the thesis take into account both wavelength-scale particles and particles larger than the wavelength of the incident light, which is important as the models used for each wavelength domain are different, and the resonance region is difficult to account for. First, the reflectance spectra of three meteorite samples are simulated using a model combining olivine, pyroxene, and iron. The results are promising as we are able to match the simulated spectra fairly well with the measured spectra. Second, spectroscopic, photometric, and polarimetric modeling of asteroid (4) Vesta shows good results as the reflectance spectra can be modeled with reasonable precision, and the modeled photometry and polarimetry produce non-linear brightening and negative degree of linear polarization in the backscattering direction that is also seen in the observations.

Finally, asteroid taxonomic classification is analysed by performing lightcurve inversion for 491 asteroids using convex and ellipsoid shapes. We retrieve phase curve slope parameters, rotation periods, pole orientations, shapes, reference phase curves, and absolute magnitudes in the G band of the ESA Gaia space telescope. Our analysis indicates that there can be mis-classifications in the current taxonomic systems. Asteroid photometry complements the existing classifications based on spectroscopy and provides us with a way to find the correct taxonomy.

The forward methods of modeling the scattering properties of surfaces used in the thesis are vital in future studies as they can be applied to other Solar System objects, such as comets and satellite surfaces. Furthermore, retrieving the scattering properties of asteroid surfaces plays a vital role in the future space missions, including asteroid mining.

Asteroid lightcurve inversion is useful especially when carrying out taxonomic classification as it provides additional information on the physical properties of the surface. The upcoming Gaia Data Release 3 will be extensive enough for rotational pole retrievals and will improve our current knowledge of the asteroids' physical properties.

Acknowledgements

This work could not have been completed without the support from many people. First, I am deeply grateful to my primary supervisor, Professor Karri Muinonen, for his guidance, wisdom, and endless patience. I also thank my secondary supervisor, Dr. Antti Penttilä, for all the feedback and guidance he has provided. Thank you to the Planetary System Research group at the University of Helsinki for providing a good working environment.

I thank my two pre-examiners, Professor Jürgen Schmidt and Dr. Javier Licandro, for their constructive comments, as well as Dr. Faith Vilas for agreeing to be the opponent.

An important part of my doctoral studies has been working at the Nordic Optical Telescope on La Palma, in the Canary Islands. I would like to thank the student community that kept me sane and active while I was writing my thesis and the last paper. I would especially like to mention my friend and flatmate, Nicholas Jannsen, who read the thesis and gave me helpful comments, as well as carried wine and food from the grocery store when I was too busy to do it myself. I am extremely grateful to Sergio Armas Pérez who supported me, acted as a Spanish-English translator when it was dearly needed, and gave me the extra push to finish everything in time.

Last but not least, I thank my parents, Eva and Pekka, who have been supporting me from the start. Thank you for taking care of my cat while I was on La Palma.

Publications

Paper I: Penttilä A., Martikainen J., Gritsevich M., Muinonen K., (2018), Laboratory spectroscopy of meteorite samples at UV-vis-NIR wavelengths: Analysis and discrimination by principal components analysis, *Journal of Quantitative Spectroscopy and Radiative Transfer*, 206:189–197.

Paper II: Lindqvist H., Martikainen J., Räbinä J., Penttilä A., Muinonen K., (2018), Ray optics for absorbing particles with application to ice crystals at near-infrared wavelengths, *Journal of Quantitative Spectroscopy and Radiative Transfer*, 217:329–337.

Paper III: Martikainen J., Penttilä A., Gritsevich M., Lindqvist H., Muinonen K., (2018), Spectral modeling of meteorites at UV-vis-NIR wavelengths, *Journal of Quantitative Spectroscopy and Radiative Transfer*, 204:144–151.

Paper IV: Martikainen J., Penttilä A., Gritsevich M., Videen G., Muinonen K., (2019), Absolute spectral modelling of asteroid (4) Vesta, *Monthly Notices of the Royal Astronomical Society*, 483:1952–1956.

Paper V: Väisänen T., Martikainen J., Muinonen K., (2020), Scattering of light by dense particulate media in the geometric optics regime, *Journal of Quantitative Spectroscopy and Radiative Transfer*, 241.

Paper VI: Muinonen K., Väisänen T., Martikainen J., Markkanen J., Penttilä A., Gritsevich M., Peltoniemi J., Blum J., Herranen J., Videen G., Maconi G., Helander P., Salmi A., Kassamakov I., Haeggström E., (2019), Scattering and absorption of light in planetary regoliths, *Journal of Visual Experiments*, 149.

Paper VII: Martikainen J., Muinonen K., Penttilä A., Cellino A., Wang X.-B., (2020), Asteroid absolute magnitudes and phase curve parameters from Gaia photometry, *Astronomy & Astrophysics*, submitted

List of abbreviations

MBO	Main-belt object
NEO	Near-Earth object
SMASS	Small Main-Belt Asteroid Spectroscopic Survey
ECAS	Eight-Color Asteroid Survey
RODS	Ray optics with diffuse and specular interactions
RT	Radiative transfer
CBM	Coherent backscattering mechanism
RT-CB	Radiative transfer with coherent backscattering
GRS	Gaussian random sphere
DEC	Discrete exterior calculus
LCI	Lightcurve inversion
DAMIT	Database of Asteroid Models from Inversion Techniques
Gaia DR2, Gaia DR3	Gaia Data Release 2 and 3
EI	Lightcurve inversion using ellipsoids
CXI	Lightcurve inversion using convex shapes
JPL	Jet Propulsion Laboratory

List of symbols

λ	wavelength
m, m_{re}, m_{im}	complex refractive index and its components
k	wave number
$\mathbf{I}$	Stokes vector
α	phase angle
θ	scattering angle
a	mean radius of the particle
σ_{sca}, σ_{ext}, σ_{abs}	scattering, extinction, and absorption cross sections
R_0	distance from the particle to the observer
$\tilde{\omega}$	single-scattering albedo
ℓ	mean free path length
κ_{e}	extinction coefficient
$r_{\parallel}$, $r_{\perp}$, $t_{\parallel}$, $t_{\perp}$	Fresnel coefficients
Q_{ext}	extinction efficiency
n	number density
ν	volume density

Contents

1 Introduction

Asteroids are irregularly shaped rocky Solar System bodies orbiting the Sun that formed around 4.6 billion years ago from the colliding dust particles in the protoplanetary disk. Some classes of asteroids are pristine samples of the early stages of the Solar System and provide us information on the origin, evolution, and current status of the asteroid population. The surface composition and structure of the asteroids can be studied through sample-return, flyby, or rendezvouz missions, meteorite laboratory measurements, or by carrying out observations using ground-based observatories or space telescopes. As space missions to asteroids are expensive and relatively rare, we mostly rely on remote sensing techniques and laboratory work.

Asteroids are classified based on their dynamical or physical properties. From the dynamical point of view, asteroids that are located between the orbits of Mars and Jupiter are called main-belt objects (MBOs) that form the majority of the known asteroids. Their average distance from the Sun ranges from 1.8 to 4.5 astronomical units (au), and most of them are assumed to be formed from the protoplanetary disk perturbed by Jupiter's gravitation. The vast majority of Near-Earth objects (NEOs) originate from the main belt. As their name indicates, NEOs' orbits can bring them close to the Earth which can cause an impact hazard. However, due to their close proximity they can be accessed and studied better than the more distant main-belt objects. NEOs contain rare natural resources, such as precious metals, and are suitable to be studied by radar observations. Transneptunian objects are the most distant Solar System asteroids. Their semimajor axes are greater than 30 au and they are located behind the orbit of Neptune. Transneptunian objects can be further classified into Kuiper-belt objects (semimajor axis $\leqslant$ 55 au) and scattered-disk objects (semimajor axis $>$ 55 au). Beyond the Kuiper belt and scattered disk, resides the Oort cloud that is the source of the long-period comets. The Oort cloud is thought to extend from 2,000 au to as far as 100,000 au.

The classification of asteroids based on the physical properties is associated with taxonomical systems. Taxonomy is usually based on spectroscopic measurements at optical and near-infrared regions (from 0.45 to 2.5 µm), but also photometric and polarimetric measurements can be utilized (Martikainen et al., 2020; Penttilä et al., 2005; Oszkiewicz et al., 2011). Spectroscopy is the study of the interaction of electromagnetic radiation and matter. A spectrum of an object describes how much electromagnetic radiation is scattered, absorbed, or emitted by the object at different wavelengths. Asteroid and meteorite spectra have different shapes, each feature telling a story of the composition of the object. Broad absorption bands are typical for reflectance spectra of complex minerals. Polarimetry is the study of the polarization of light and photometry measures the intensity of an asteroid's electromagnetic radiation. A photometric phase curve describes the brightness of an asteroid as a function of the phase angle (the Sun-object-observer angle) and can be used to determine the light-scattering properties of the asteroid surface, such as composition, roughness, and texture. A photometric lightcurve describes variation in magnitude with time and gives us information on the asteroid's rotation, size, and composition (Harris and Lupishko, 1989). Polarimetric measurements are often carried out at different wavelengths and contain information on the asteroid's surface composition (Penttilä et al., 2005).

The most common taxonomic systems that utilize asteroid spectra are the Tholen (Tholen, 1989) and Small Main-Belt Asteroid Spectroscopic Survey (SMASS)/Bus-DeMeo classifications (Bus and Binzel, 2002; DeMeo et al., 2009). The Tholen taxonomy is based on the broad-band spectra of 978 asteroids obtained by the Eight-Color Asteroid Survey (ECAS). A few thousand asteroids are included in the SMASS taxonomy, whereas Bus-DeMeo extends the amount of asteroids in the SMASS by 371 and the wavelength range to 2.45 µm.

Table 1.1: Tholen and Bus-DeMeo taxonomic classification (Tholen, 1989; Bus and Binzel, 2002; DeMeo et al., 2009).

	Bus-DeMeo	Tholen
S-complex	S, Sa, Sq, Sr, Sv, A, Q, K, L, R	S
C-complex	B, C, Cb, Cg, Cgh, Ch	C, B, F, G
X-complex	X, Xc, Xe, Xk	M, X, E, P
Small types	D, Ld, O, T, V	A, D, T, Q, R, V

About 75% of all known asteroids are classified into the C-complex. They are typically dark, carbon-rich, and contain hydrated minerals. Their spectral features are similar to carbonaceous chondrites that are primitive, undifferentiated meteorites containing water and organic compounds. The S-complex are the second most common asteroids, and are brighter than the C-complex. They are located in the inner part of the asteroid main belt and consist of silicates. The intrinsic brightness of the

X-complex asteroids is approximately equal to the S-complex. In the Tholen classification, X-complex is divided into M, X, E, and P types. The mineralogy within the X-complex varies significantly, however, M types are assumed to typically contain nickel-iron, whereas enstatite is common in E types. The most significant asteroids classified under small types is the V type that originates from (4) Vesta. V types are similar to S types both chemically and in brightness, however, they contain more pyroxene that leaves its own signature in the spectra.

When interpreting remote-sensing data, we must understand light scattering by a regolith, a layer of small grains covering the asteroid's surface. However, this is not a simple task as light scattering by small Solar System bodies is not fully understood and remains an open problem. Observations are affected by the geometry of the object, the Earth's atmospheric effects, and physical and chemical composition of the regolith. Furthermore, asteroids are under constant bombardment of micrometeoroids, solar wind, and cosmic rays that create nano-scale iron particles on the surface. This alteration, known as space weathering, decreases the albedo, as well as reddens and flattens the spectral features (Clark et al., 2002; Penttilä et al., 2020).

Laboratory studies are essential when trying to understand the light scattering physics involved. Meteorites are almost untouched samples of their parent bodies and examining them in a well-controlled environment gives us information on their parent asteroids' composition and structure. Several studies have created samples that mimic asteroid, comet, lunar, and martian surfaces in order to understand their light-scattering properties. However, creating realistic samples can be challenging due to the laboratory environment being very different from that in space. Asteroids are surrounded by vacuum and affected by space weathering and collisions between other asteroids, moreover, meteorite surfaces are free of regolith that forms on asteroid surfaces in low gravity. These conditions must be somehow taken into account (Tang et al., 2012; Kohout et al., 2014). Another approach is to study the most common materials that dominate asteroid spectra (such as olivine, pyroxene, carbon, and iron) and, for example, retrieve their refractive indices that can be further used in light-scattering simulations.

There are multiple approaches to model light scattering by asteroid regoliths. The most commonly used model favored by many planetary scientists is the Hapke model (Hapke, 1963; Hapke, 2008) that was named after its developer Bruce Hapke. Many studies have shown that using the model is feasible when standardizing remote sensing data (Simonelli et al., 1996) but the limitations of the model become prominent when using it to characterize light-scattering properties: the model parameters describing particle sizes or roughness become unrealistic (Shepard and Helfenstein, 2007).

Numerical methods that are based on the Maxwell equations are widely used to interpret observational data and laboratory measurements. These methods require real physical properties as input parameters, such as the volume fraction of the particles, shape and size distribution, and complex refractive indices. Exact methods that solve the Maxwell equations are mostly inapplicable when modeling asteroid regoliths due to the amount of particles and wavelengths in the system, and the restrictions the computing capacity sets (Egel et al., 2017). To make the computations faster and less demanding, approximate multiple scattering methods, such as ray-tracing with geometric optics approximation (Stankevich and Shkuratov, 2002; Muinonen et al., 1996; Väisänen et al., 2020), are used.

In this thesis, I have developed and utilized robust numerical methods to characterize light-scattering properties of meteorites and asteroids at UV-Vis-NIR wavelengths. The experimental methods carried out in this thesis included spectroscopic measurements of various samples.

In Chapter 2, I present briefly the basic scattering theory and concepts behind the numerical methods. In Chapter 3, I introduce the light-scattering codes used in the simulations, and in Chapter 4, I describe the simulation frameworks used to model meteorites and asteroids in more detail. The author's contributions and included papers are summarized in Chapter 5. Chapter 6 is dedicated to the concluding remarks, and finally, Papers I–VII are presented.

2 Light scattering

In the following, I present a brief introduction to the light-scattering theory behind the methods used in the scattering simulations in Chapter 4.

2.1 Inhomogeneous waves

The Maxwell equations can be written as in Griffiths (2013),

$$\begin{aligned}\nabla \cdot \mathbf{D}(\mathbf{r}, t) &= \rho_f(\mathbf{r}, t), \\ \nabla \cdot \mathbf{B}(\mathbf{r}, t) &= 0, \\ \nabla \times \mathbf{E}(\mathbf{r}, t) &= -\frac{\partial \mathbf{B}(\mathbf{r}, t)}{\partial t}, \\ \nabla \times \mathbf{H}(\mathbf{r}, t) &= \mathbf{J}_f(\mathbf{r}, t) + \frac{\partial \mathbf{D}(\mathbf{r}, t)}{\partial t},\end{aligned} \tag{2.1}$$

with **D** describing the electric field displacement, **H** and **E** describing the magnetic and electric fields, **B** describing the magnetic flux density, and $\mathbf{J}_f$ and ρ_f describing the free-current and free-charge densities. By using Eq. 2.1 and by assuming a non-magnetic medium, charge-free and current-free system, we can find a solution for the plane wave $\mathbf{E}(\mathbf{r}, t)$:

$$\mathbf{E}(\mathbf{r}, t) = \mathbf{E}_0 \exp(\mathrm{i}\mathbf{k} \cdot \mathbf{r} - \mathrm{i}\omega t), \tag{2.2}$$

where $\mathbf{E}_0$ is a constant, and ω is the angular frequency. In an absorbing medium, **k** is the wave vector

$$\mathbf{k} = k(N\hat{\mathbf{e}} + \mathrm{i}K\hat{\mathbf{f}}), \tag{2.3}$$

in which N and K are medium-specific, apparent refractive indices, k is the wave number $k = 2\pi/\lambda$ with λ denoting the wavelength, and $\hat{\mathbf{f}}$ and $\hat{\mathbf{e}}$ being the unit normals to the planes of constant amplitude and phase (Dupertuis et al., 1994; Chang et al., 2005). The optical properties of a material are described with the complex refractive index $m = m_{\rm re} + {\rm i}m_{\rm im}$. The real part of the refractive index, $m_{\rm re}$, is the ratio of the speed of light in free-space and the phase velocity of an electromagnetic wave in the medium. The imaginary part, $m_{\rm im}$, relates to the absorption in the medium. According to Chang et al. (2005), in the case of $m_{\rm im}/m_{\rm re} > 0.01$, inhomogeneous waves ($\hat{\mathbf{e}} \cdot \hat{\mathbf{f}} \neq 0$) need to be considered. By substituting $\mathbf{k}$ in Eq. 2.2, we obtain an equation describing the inhomogeneous plane waves:

$$\mathbf{E}(\mathbf{r}, t) = \mathbf{E}_0 \exp(-kK\hat{\mathbf{f}} \cdot \mathbf{r}) \exp({\rm i}kN\hat{\mathbf{e}} \cdot \mathbf{r} - {\rm i}\omega t). \tag{2.4}$$

2.2 Basic definitions

When considering far fields in free space, the electric field can be presented with components parallel ($E_{||}$) and perpendicular ($E_{\perp}$) to the scattering plane (Bohren and Huffman, 1983) :

$$\mathbf{E} = E_{||}\hat{\mathbf{e}}_{||} + E_{\perp}\hat{\mathbf{e}}_{\perp} \tag{2.5}$$

that can be further related to a Stokes vector that describes the polarization of radiation and consists of four Stokes parameters

$$\mathbf{I} = \begin{pmatrix} I \\ Q \\ U \\ V \end{pmatrix} = \begin{pmatrix} \langle E_{||}E_{||}^* + E_{\perp}E_{\perp}^* \rangle \\ \langle E_{||}E_{||}^* - E_{\perp}E_{\perp}^* \rangle \\ \langle E_{||}E_{\perp}^* + E_{\perp}E_{||}^* \rangle \\ {\rm i}\langle {\rm E}_{||}{\rm E}_{\perp}^* - {\rm E}_{\perp}{\rm E}_{||}^* \rangle \end{pmatrix}, \tag{2.6}$$

in which I is the intensity of light, Q and U are the linear polarization states, and V is the circular polarization state. For unpolarized light, $Q = U = V = 0$, for fully polarized light $I^2 = Q^2 + U^2 + V^2$, and for partially polarized light $I^2 > Q^2 + U^2 + V^2 > 0$. The degree of polarization p is written as

$$p = \frac{\sqrt{Q^2 + U^2 + V^2}}{I}. \tag{2.7}$$

A scattering event can change the state of the incident light. This change is fully described in a 4×4 Mueller matrix that is called a scattering matrix or a scattering, phase matrix depending on how it is scaled. The 4×4 matrix is a function of the scattering angle θ or the phase angle $\alpha = \pi - \theta$, and depends on the orientation of the particle when the particle is asymmetric.

After a light beam interacts with an object, part of it can either scatter or be absorbed. Multiple factors affect the amount of scattering and absorption: size and

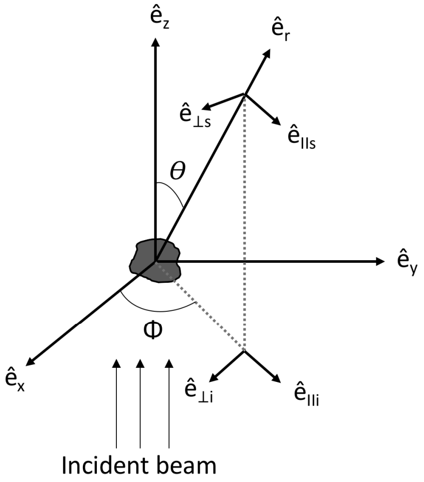

Figure 2.1: Geometry of light scattering event by an irregular particle following Bohren and Huffman (1983).

shape of the object, optical properties (such as the complex refractive index), and the wavelength of the incident light. A scattering event can be described with the help of the scattering matrix **S**:

$$\begin{pmatrix} I_{\mathrm{sca}} \\ Q_{\mathrm{sca}} \\ U_{\mathrm{sca}} \\ V_{\mathrm{sca}} \end{pmatrix} = \frac{1}{k^2 R_0^2} \begin{pmatrix} S_{11} & S_{12} & S_{13} & S_{14} \\ S_{21} & S_{22} & S_{23} & S_{24} \\ S_{31} & S_{32} & S_{33} & S_{34} \\ S_{41} & S_{42} & S_{43} & S_{44} \end{pmatrix} \begin{pmatrix} I_{\mathrm{inc}} \\ Q_{\mathrm{inc}} \\ U_{\mathrm{inc}} \\ V_{\mathrm{inc}} \end{pmatrix}. \tag{2.8}$$

For sunlight (unpolarized), the scattered intensity relates to the component S_{11}. When studying light scattering by planetary surfaces, we are mainly interested in the phase function $S_{11}(\alpha)$ and the degree of linear polarization $-S_{21}(\alpha)/S_{11}(\alpha)$.

The physical size of an object can be defined using a size parameter $x = ka$, where k is the wave number and a is the mean radius. Depending on the real part of the refractive index m_{re}, light scattering can be divided into different regions. With $m_{\mathrm{re}} \approx 1.5$, the three main regions are geometric optics ($x >> 1$), resonance ($x \approx 1$) and Rayleigh ($x << 1$). In the thesis, geometric optics and resonance regions are studied, whereas the Rayleigh region is not relevant for regolith particles at Vis-NIR wavelengths and is thus omitted from the simulations.

2.3 Ray optics

Light scattering by particles that are larger than the wavelength of the incident light can be solved with the help of ray optics. The 4 × 4 phase matrix **P** is given by

$$\mathbf{P} = \frac{4\pi}{k^2 \sigma_{\mathrm{sca}}} \mathbf{S}, \tag{2.9}$$

where σ_{sca} is the ensemble-averaged scattering cross section that describes the total scattered power and **S** is the 4 × 4 scattering matrix. The incident and scattered Stokes vectors $\mathbf{I}_{\mathrm{inc}}$ and $\mathbf{I}_{\mathrm{sca}}$ are related as

$$\mathbf{I}_{\mathrm{sca}} = \frac{\sigma_{\mathrm{sca}}}{4\pi R_0^2} \mathbf{P} \mathbf{I}_{\mathrm{inc}}, \tag{2.10}$$

in which R_0 is the distance from the particle to the observer, and **P** is normalized as

$$\int_{4\pi} \frac{d\Omega}{4\pi} P_{11} = 1. \tag{2.11}$$

Considering particles that are larger than the wavelength, σ_{sca} can be divided into a ray-tracing part σ^{RT} and a forward-diffraction part σ^{D} (Muinonen et al., 2009):

$$\sigma_{\mathrm{sca}} = \sigma_{\mathrm{sca}}^{\mathrm{D}} + \sigma_{\mathrm{sca}}^{\mathrm{RT}}. \tag{2.12}$$

The extinction cross section σ_{ext} can be written as

$$\sigma_{\mathrm{ext}} = \sigma_{\mathrm{abs}} + \sigma_{\mathrm{sca}} \tag{2.13}$$

with σ_{abs} describing the absorption cross section. The single-scattering albedo $\tilde{\omega}$ is

$$\tilde{\omega} = \frac{\sigma_{\mathrm{sca}}}{\sigma_{\mathrm{ext}}}. \tag{2.14}$$

Following the geometric-optics treatment for external incidence, Snel's law is applied in the form

$$\sin\theta_i = \mathrm{Re}(m) \sin\theta_\tau, \tag{2.15}$$

where θ_τ and θ_i are the angles of refraction and incidence. The Mueller matrices for refracted and reflected rays are

$$\begin{aligned} \mathbf{M}_{\mathrm{R}} &= \mathbf{R} \cdot \mathbf{K} \cdot \mathbf{M}_{\mathrm{inc}}, \\ \mathbf{M}_{\mathrm{T}} &= \mathbf{T} \cdot \mathbf{K} \cdot \mathbf{M}_{\mathrm{inc}}, \end{aligned} \tag{2.16}$$

in which $\mathbf{K}$ is the rotation to the plane of incidence, and $\mathbf{R}$ and $\mathbf{T}$ are the Fresnel reflection and transmission matrices (Muinonen et al., 1996):

$$\mathbf{K} = \begin{bmatrix} 1 & 0 & 0 & 0 \\ 0 & \cos 2\psi & \sin 2\psi & 0 \\ 0 & -\sin 2\psi & \cos 2\psi & 0 \\ 0 & 0 & 0 & 1 \end{bmatrix},$$

$$\mathbf{T} = \frac{1}{2} \begin{bmatrix} t_{\parallel}t_{\parallel}^{*} + t_{\perp}t_{\perp}^{*} & t_{\parallel}t_{\parallel}^{*} - t_{\perp}t_{\perp}^{*} & 0 & 0 \\ t_{\parallel}t_{\parallel}^{*} - t_{\perp}t_{\perp}^{*} & t_{\parallel}t_{\parallel}^{*} + t_{\perp}t_{\perp}^{*} & 0 & 0 \\ 0 & 0 & 2\mathrm{Re}(t_{\parallel}t_{\perp}^{*}) & 2\mathrm{Im}(t_{\parallel}t_{\perp}^{*}) \\ 0 & 0 & -2\mathrm{Im}(t_{\parallel}t_{\perp}^{*}) & 2\mathrm{Re}(t_{\parallel}t_{\perp}^{*}) \end{bmatrix},$$

$$\mathbf{R} = \frac{1}{2} \begin{bmatrix} r_{\parallel}r_{\parallel}^{*} + r_{\perp}r_{\perp}^{*} & r_{\parallel}r_{\parallel}^{*} + r_{\perp}r_{\perp}^{*} & 0 & 0 \\ r_{\parallel}r_{\parallel}^{*} + r_{\perp}r_{\perp}^{*} & r_{\parallel}r_{\parallel}^{*} + r_{\perp}r_{\perp}^{*} & 0 & 0 \\ 0 & 0 & 2\mathrm{Re}(r_{\parallel}r_{\perp}^{*}) & 2\mathrm{Im}(r_{\parallel}r_{\perp}^{*}) \\ 0 & 0 & -2\mathrm{Im}(r_{\parallel}r_{\perp}^{*}) & 2\mathrm{Re}(r_{\parallel}r_{\perp}^{*}) \end{bmatrix}. \tag{2.17}$$

Here ψ denotes the rotation angle, whereas $r_{\parallel}$, $r_{\perp}$, $t_{\parallel}$ and $t_{\perp}$ are Fresnel coefficients

$$r_{\parallel} = \frac{m\cos\theta_i - \cos\theta_t}{m\cos\theta_i + \cos\theta_t}, \quad r_{\perp} = \frac{\cos\theta_i - m\cos\theta_t}{\cos\theta_i + m\cos\theta_t},$$

$$t_{\parallel} = \frac{2\cos\theta_i}{m\cos\theta_i + \cos\theta_t}, \quad t_{\perp} = \frac{2\cos\theta_i}{\cos\theta_i + m\cos\theta_t}. \tag{2.18}$$

The internal and external incidences are treated the same way, however, the internal incidence allows the rays to be totally reflected or attenuated.

In this thesis, I use ray optics with diffuse and specular interactions (RODS) developed by Muinonen et al. (2009), Lindqvist et al. (2018), and Martikainen et al. (2018) where rays are traced until a specific number of reflections and/or refractions and/or diffuse scattering events are performed. To address internal inhomogeneities, diffuse scattering from small internal scatterers is taken into account. This is done using the scattering phase matrix, single scattering albedo, and extinction mean free-path length ℓ (the average distance traveled by the ray):

$$\ell = \frac{1}{\kappa_{\mathrm{e}}}, \tag{2.19}$$

where κ_{e} is the extinction coefficient written as

$$\kappa_{\mathrm{e}} = nQ_{\mathrm{ext}}\pi a_0^2 = \frac{3\nu Q_{\mathrm{ext}}}{4a_0}, \tag{2.20}$$

in which Q_{ext} is the extinction efficiency, n is the number density, and ν is the volume density. In Paper V, extinction distance distributions are used instead of a single value for the extinction mean free path. The diffuse scattering treatment is explained in detail by Muinonen et al. (2009).

2.4 Coherent backscattering

Multiple studies have shown that at the opposition (when the phase angle approaches zero) the asteroid surface intensity peaks, and the degree of linear polarization shows a negative surge (e.g. Gehrels et al., 1964; Shkuratov et al., 2002). This phenomenon is known as the opposition effect and for a long time it was not properly understood. The strength of the opposition brightening depends on the surface properties. At first, it was thought that the regolith particles shadowing each other are the source of the effect (Hapke, 1963) but later studies have shown that the coherent backscattering mechanism (CBM) plays a part (Shkuratov, 1988; Muinonen, 1990; Muinonen et al., 2011). CBM is caused by a constructive interference between two waves traveling the same paths but in opposite directions. The effect is significant near the backscattering direction (Mishchenko et al., 2006) and needs to be accounted for when modeling light scattering by asteroid surfaces. The phase difference $\Delta\phi$ between these waves in opposite paths is given by the positions of the first and last scatterers $\mathbf{r}_0$ and $\mathbf{r}_n$, and the directions of the scattered and incident field $\hat{\mathbf{k}}_f$ and $\hat{\mathbf{k}}_i$:

$$\Delta\phi = k(\hat{\mathbf{k}}_f + \hat{\mathbf{k}}_i) \cdot (\mathbf{r}_n - \mathbf{r}_0). \tag{2.21}$$

2.5 Particle shapes

In order to simulate light scattering by different surfaces, we need to define the shapes and sizes of the surface particles that interact with the incident light. This can be quite challenging as on planetary surfaces the particle shapes and sizes are unknown

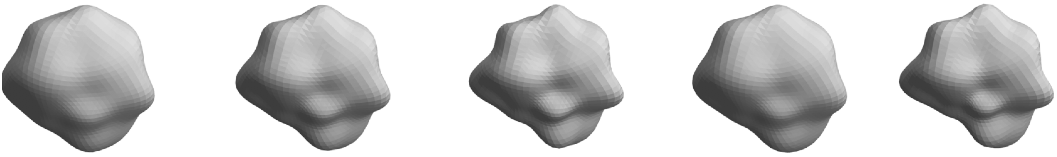

Figure 2.2: A collection of Gaussian-random-sphere particles.

and differ from one particle to another. However, with some random particle models and size distributions, we can simulate the surface with reasonable accuracy. In this thesis, particles that are larger than the wavelength are simulated using Gaussian random spheres (GRS). As wavelength-scale non-spherical particles scatter the light most effectively in the resonance domain, we introduce Voronoi particles to include faceted particles suitable for producing volume elements.

2.5.1 Gaussian-random-sphere particles

A GRS is defined as an infinite ensemble of sample particles that is obtained from the probability density function for the Gaussian random sphere $\mathbf{r} = r(\theta, \phi)\mathbf{e}_r$ that is described in spherical coordinates (θ, ϕ). GRS particles are widely used in light-scattering simulations as they are statistically well-defined irregularly-shaped particles that can be easily generated using the following equations (Muinonen et al., 2009):

$$r(\theta, \phi)\mathbf{e}_r = \frac{a\exp[s(\theta, \phi)]}{\sqrt{1+\sigma^2}}\mathbf{e}_r,$$

$$s(\theta, \phi) = \sum_{l=0}^{\infty} \sum_{m=-l}^{l} s_{lm} Y_{lm}(\theta, \phi),$$

$$s_{l,-m} = (-1)^m s^*_{lm}, \tag{2.22}$$

where $s = s(\theta, \phi)$ is the logarithmic radial distance, σ is the relative standard deviation, a is the mean standard deviation for the radial distance, s_{lm} are the Gaussian random variables with zero means, and Y_{lm} are the orthonormal spherical harmonics.

The standard deviations of $\mathrm{Re}(s_{lm})$ and $\mathrm{Im}(s_{lm})$ are obtained from the covariance function Σ_s for the random variables. The covariance function describes the autocovariance of the random variables $s(\vartheta_1, \varphi_1)$ and $s(\vartheta_2, \varphi_2)$, and is obtained from a series of Legendre polynomials P_l:

$$\Sigma_s(\gamma) = \sum_{l=0}^{\infty} C_l P_l(\cos\gamma), \qquad \sum_{l=0}^{\infty} C_l = \log_e(1+\sigma^2) \tag{2.23}$$

where γ is the angular distance and the coefficients $C_l \geqslant 0 (l = 0, ..., \infty)$. The random variables s_{lm} are written as

$$s_{lm} = \sqrt{\frac{2\pi C_l}{2l+1}} \left(x_{\mathrm{G}} \sqrt{1+\delta_{m0}} + \mathrm{i} y_{\mathrm{G}} \sqrt{1-\delta_{m0}} \right),$$
$$l = 0, 1, ..., \infty, \qquad m = 0, 1, ..., l, \tag{2.24}$$

in which x_{G} and y_{G} are Gaussian random variables with zero means and standard deviations that equal to unity.

Parameters describing the Gaussian random sphere are a and C_l. By choosing the power-law covariance function, C_l can be further parameterized:

$$C_0 = C_1 = 0, \tag{2.25}$$

$$C_l = \frac{\widetilde{C}}{l^{\nu_0}}, l = 2, 3, ..., l_{\max}, \tag{2.26}$$

$$\widetilde{C} \sum_{l=2}^{l_{\max}} \frac{1}{l^{\nu_0}} = \log_e(1+\sigma^2) \Rightarrow \widetilde{C} = \log_e(1+\sigma^2) \left[\sum_{l=2}^{l_{\max}} \frac{1}{l^{\nu_0}} \right]^{-1}, \tag{2.27}$$

in which $\widetilde{C}$ is a normalization constant, and the standard deviation σ and the power law index ν_0 are statistical shape parameters.

2.5.2 Voronoi particles

Voronoi tesselation is a space partition where the cells are defined as volumes of shortest possible distance to the seed point of that cell. The so-called Voronoi particles, which consist of these Voronoi cells, can be generated using an algorithm introduced by Markkanen et al. (2015) and Zubko et al. (2009). The algorithm generates a Voronoi-partitioned sphere that consists of Voronoi cells made of tetrahedral elements. Large-scale irregular structure is created by removing Voronoi cells that touch the surface of the sphere. Porosity is added to the particle by randomly removing cells using the porosity parameter. Additionally, inhomogeneities can be included by randomly choosing the complex refractive index with a given probability for each Voronoi cell.

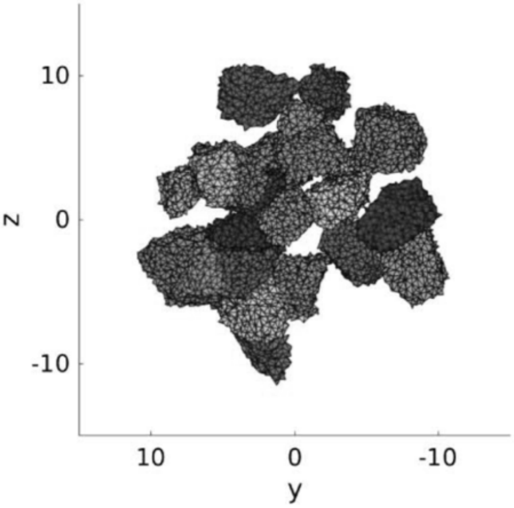

Figure 2.3: A Voronoi particle consisting of Voronoi cells.

2.6 Asteroid photometric models

Asteroid photometry provides us with information on the physical properties and composition of the surface. Phase curves are mostly linear in the magnitude scale except close to the backscattering direction, where a brightness surge can be seen. Obtaining a phase curve requires the retrieval of an asteroid's rotational lightcurves over a range of phase angles with high photometric accuracy. Fitting a phase function to the obtained apparent magnitudes and the corresponding phase angles gives the absolute magnitude and photometric parameters. Absolute magnitude is the magnitude value at zero phase angle and the photometric slope parameter describes how steep the phase function is. These quantities are related to the asteroid's taxonomic class, geometric albedo, porosity, particle size distribution, and packing density. In the thesis, we use the H, G_1, G_2 and H, G_{12} phase functions developed by Muinonen et al. (2010) to retrieve absolute magnitudes and phase curve slope parameters. The H, G_1, G_2 phase function is designed for extensive and accurate photometric data spanning small and large phase angles, whereas the H, G_{12} phase function is designed for limited ranges of phase angles and is thus useful when interpreting the Gaia observations.

3 Light-scattering codes

Light scattering by planetary surfaces can be simulated with various different computational methods that each have their own strengths and weaknesses. Some codes are fast, some are built for accuracy but have limitations regarding the computational demands, some use only specific, simplified scattering geometries and sizes. There is no single code that is applicable to every case. Depending on what we want to model and what computational capacities are available, we must choose the methods that are best suited to solve the light-scattering problem at hand. The codes used in this thesis are SIRIS, JVIE, RT-CB, and LCI which are described in more detail below. SIRIS, JVIE, and RT-CB are based on forward methods that numerically derive what should be observed, whereas LCI uses inverse methods, in which the physical properties are obtained from the observations by inverting the model parameters.

3.1 Forward methods

3.1.1 SIRIS

SIRIS is a geometric optics code originally developed by Muinonen et al. (2009). It is a ray tracer that uses the classical Snel's law and the Fresnel reflection and refraction matrices to retrieve scattering properties of the GRS particles with or without internal diffuse scatterers.

In a strongly absorbing medium, the electromagnetic waves are inhomogeneous, implicating that the amplitude and phase vectors do not generally coincide (Epstein, 1930). This means that Snel's law and the Fresnel's equations should not be used in their classical forms that only account for the real-valued variables. Furthermore, the attenuation of radiation caused by absorption cannot be computed using a simple exponential attenuation along the ray path as it does not account for the inhomogeneous waves. Chang et al. (2005) showed that if the inhomogeneous nature of waves is omitted from the simulations, it causes errors. To correct these errors, we implemented inhomogeneous waves with a generalized Snel's law (Dupertuis et al.,

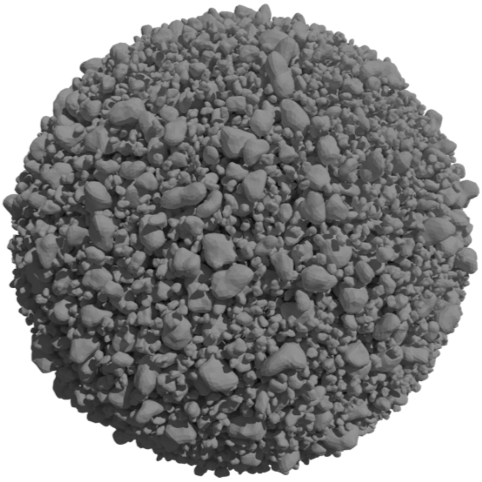

Figure 3.1: An example scattering medium consisting of GRS particles with a power-law size distribution.

1994) into the new SIRIS4 (see Paper II), that was further upgraded in Paper III with the implementation of diffuse scatterers.

SIRIS4 generates multiple rays outside the scattering medium. The rays hit the surface of the particle where they can be reflected and refracted. In case diffuse scatterers are included within the particle, the rays that enter the medium can scatter diffusively and change the direction of propagation. In an absorbing medium, radiation is attenuated along the ray path, and if the intensity of a ray drops below a specified cutoff limit it will be killed. The user-defined input contains the shape, size, and optical properties (such as the complex refractive index) of the particle, wavelength of the light, and the volume fraction and scattering properties of the diffuse scatterers.

The latest framework of SIRIS uses arbitrary meshes that describe the scattering medium (see Paper V). The meshes are created by placing particles randomly inside a periodic box. The volume is iteratively shrunk towards a desired volume fraction while randomly moving the particles and allowing them to pack more tightly. Different scattering medium geometries can then be extracted from the box (see Fig. 3.1). This version supports various materials with or without diffuse scatterers.

3.1.2 JVIE

JVIE is an electric-current volume-integral equation solver developed by Markkanen et al. (2012) that computes light-scattering properties of irregularly shaped particles. It uses geometries that consist of tetrahedral elements and solves the T-matrix (Waterman, 1965) that describes the light-scattering characteristics of the scattering medium. JVIE uses numerically exact methods to solve the Maxwell equations, and is thus computationally demanding. In Paper VI, JVIE was used to simulate Voronoi-shaped particles in the resonance domain.

3.1.3 Radiative Transfer with Coherent Backscattering

Radiative Transfer with Coherent Backscattering (RT-CB) is an approximate method developed by Muinonen (2004). It generates multiple rays with different Stokes parameters, traces them within the diffuse medium, and computes the scattering matrix of the medium. The rays travel inside the medium until an interaction with a diffuse scatterer changes the direction of the propagation.

In RT-CB, every diffuse scattering event generates rays that are peeled off and collected outside the medium. The collected intensity is subtracted from the original ray that keeps propagating and diffusely scattering inside the medium until its intensity drops below the cutoff limit. The CB part is computed so that after a diffuse scattering event, another ray is similarly traced in the reverse order. In Paper VI, we collected the averaged scattering matrix computed with SIRIS, and the amplitude scattering matrix computed with JVIE into a single averaged scattering phase matrix which was then modified into the form of a pure Mueller matrix as an input for the RT-CB simulations.

3.2 Inverse methods

3.2.1 LCI

Lightcurve inversion (LCI) is an algorithm developed by Muinonen et al. (2020), see also Kaasalainen et al. (1992) and Lamberg (1993), that uses triaxial ellipsoid (EI) or general convex shapes (CXI) to retrieve rotation periods, pole orientations, shapes, and phase curve parameters from lightcurve observations.

For CXI, the given input vector is $\mathbf{P} = (P, \lambda, \beta, \phi_0, s_{00}, ..., s_{l_{\max}l_{\max}}, p, G_1, G_2, D)^{\mathrm{T}}$, where the parameters are rotation period, ecliptic pole longitude, ecliptic pole latitude, rotational phase at a given epoch t_0, shape parameters $s_{00}, ..., s_{l_{\max}l_{\max}}$, geometric albedo p, G_1 and G_2 parameters of the H, G_1, G_2 phase function, and the diameter D. In the case of the EI, the parameters are $\mathbf{P} = (P, \lambda, \beta, \phi_0, a, b, c, p, G_1, G_2, D)^{\mathrm{T}}$, in which a, b, and c are the ellipsoid semiaxes. For both inverse methods, the geometric albedo and the diameter are omitted from the model. Additionally, the rotational phase ϕ_0 is an unnecessary input parameter in CXI since it is being accounted for in the model.

First, LCI uses Levenberg-Marquardt least-squares optimization method (for CXI) or the Nelder-Mead downhill simplex algorithm (for EI) to find the best-fit spin, shape, and scattering parameters for the given observations. Second, virtual observations are generated by adding Gaussian random errors to the actual observations, and the Levenberg-Marquardt optimization or the Nelder-Mead downhill simplex algorithm is used to find their best-fit spin, shape, and scattering parameters. Finally, Markov-Chain Monte Carlo -method is performed with the help of the virtual least-squares solutions to sample the spin, shape, and scattering parameters.

4 Modeling the surface

When modeling planetary materials, there are several aspects to consider. Our free samples of the Solar System, meteorites, are small in size, and their surfaces differ significantly from those of asteroids. Asteroid regolith is known to consist of particles of various sizes, shapes, and optical properties packed in low gravity, whereas those meteorites that remain in our collections are solid pieces of rock. In this thesis, I introduce new methods to model the reflectance spectra of various meteorite surfaces, and then proceed to study the spectroscopy, photometry, and polarimetry of asteroid regoliths.

4.1 Meteorite mineralogy

Meteorites are divided into groups based on their structure, mineralogy, and chemical and isotopical composition (Clayton and Mayeda, 1989). The majority of meteorites are classified into chondrites or achondrites. Chondrites are stony meteorites that contain chondrules, small particles consisting of silicate minerals olivine and pyroxene.

Chondrites can be further divided into enstatite chondrites, ordinary chondrites, carbonaceous chondrites, kakangari chondrites, and rumuruti chondrites. Enstatite chondrites are rare meteorites that have a high abundancy of enstatite mineral. Ordinary chondrites are the most common type of meteorite to fall to Earth, and they contain Fe-Ni metal and troilite. Ordinary chondrites are further divided into H chondrites (high total iron and high metal contents), L chondrites (low total iron content), and LL chondrites (low total iron and low total metal contents). Carbonaceous chondrites are rich in carbon and they typically contain water or minerals altered by water. Kakangari chondrites and rumuruti chondrites are very rare as only a few meteorites have been classified into one of the groups. The petrologic and oxygen isotopic charasteristics of Kakangari chondrites are unique and distinguishable from other chondrites (Weisberg et al., 1996). Rumuruti chondrites are oxidized, contain little Fe-Ni and are assumed to originate from a regolith of an asteroid.

Achondrites are stony meteorites that do not contain chondrules. Their parent asteroid has typically experienced melting and differentiation, and their material is similar to terrestrial basalts. Achondrites are divided into primitive achondrites, asteroidal achondrites, Lunar achondrites, and Martian achondrites. Asteroidal achondrites are further divided into HED meteorites, angrites, and aubrites. The majority of achondrites are from the HED group that consists of howardites, eucrites, and diogenites, and is assumed to originate from asteroid (4) Vesta (McSween et al., 2013). Eucrites contain pyroxene-rich basaltic rock from the crust of Vesta, whereas diogenites are rich in orthopyroxene originating from deeper parts of Vesta's crust. Howardites typically contain fragments of eucrite and diogenite. Angrites contain mostly augite mineral, whereas aubrites consist of orthopyroxene enstatite.

In our simulation framework (see Paper III), we have utilized clinopyroxene, bronzite (orthopyroxene), olivine, and iron. Pyroxenes are minerals abundant in basalts that contain mostly calcium, iron, and magnesium. Pyroxenes can be divided into clinopyroxenes and orthopyroxenes based on how they crystallize. Olivine is a common mineral on Earth that contains magnesium, iron, and silicates.

4.2 Meteorite spectroscopy

Meteorites travel a long way before they reach the ground: typically their journey starts after an impact releases them from the surface of their parent asteroid. Collisions between asteroids produce shockwaves that fragment the surface creating pockets and veins filled with shock-melted materials, such as sulfides and metallic iron (Kohout et al., 2014). After its release from the parent asteroid, the meteorite experiences space weathering that alters its surface properties, until it finally enters the Earth's atmosphere that melts its outer layer forming a fusion crust. If not collected immediately, physical and chemical terrestrial weathering starts to alter the surface. Here, I present the experimental and numerical methods to simulate the spectral properties of meteorite samples.

4.2.1 Experimental methods

In Paper I, we measured the reflectance spectra of 30 meteorite samples with the University of Helsinki integrating-sphere UV-Vis-NIR spectrometer that has a quartz tungsten-halogen and a deuterium light source. The incoming light was collected using a 2.5-mm circular aperture, and a 2.5-mm rectangular slit. The wavelength range of the measurements was from 250 to 2500 nm with 5-nm sampling steps. Our meteorite sample collection was borrowed from the Finnish Museum of Natural History,

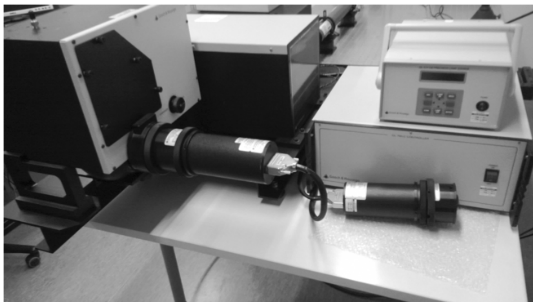

Figure 4.1: The University of Helsinki UV-Vis-NIR spectrometer.

and contained 23 ordinary chondrites, 4 HED meteorites, one aubrite, one carbonaceous chondrite, and one enstatite. The measured surfaces were either polished or unpolished, and free of fusion crust.

4.2.2 Retrieval of complex refractive indices

Our light-scattering methods require the complex refractive indices as the material parameter, and thus they need to be retrieved for the modeled wavelength region. This is usually a problem because only a few materials have well-defined complex optical properties that can be found from existing databases. To model the meteorite spectra, we wanted to use three of the most common materials that dominate their spectral features: olivine, pyroxene, and iron. The complex refractive indices of olivine and iron could be found from Jena Database of Optical Constants for Cosmic Dust and Refractiveindex.info. However, we could not find the optical constants for pyroxene. For our modeling purposes, we developed an optimization algorithm that uses the measured reflectance spectra of the material and SIRIS4 with GRS shapes to derive the imaginary part of the complex refractive index m_{im}. First, the method was validated by deriving the m_{im} for clinopyroxene and then further applied to retrieve the m_{im} of bronzite that was used in the spectral model. The optimization algorithm is described in detail in Paper III. The validation of the m_{im} with clinopyroxene shows that the obtained m_{im} is not grain-size specific, and can be used to model various sizes with high precision (see Fig. 4.6).

4.2.3 Spectroscopic model

In Paper III, we used the measured spectra of Kisvarsany (H ordinary chondrite), Johnstown (Diogenite), and St. Germain du Pinel (L ordinary chondrite) meteorites

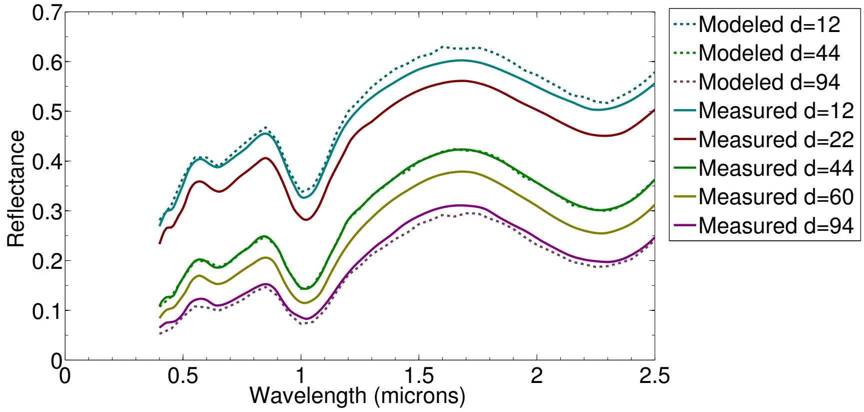

Figure 4.2: The spectra of clinopyroxene modeled with the derived m_{im} for different grain sizes.

Figure 4.3: The Kisvarsany, Johnstown, and St. Germain du Pinel meteorite samples.

to model their spectral features. All of the samples were "falls", collected after their fall through the atmosphere was observed. The measured surfaces were unpolished and free of fusion crust.

For this work, SIRIS4 was updated to account for diffuse scatterers that constitute an internal medium spanning uniformly across the particle interior. We modeled the meteorite spectra so that small iron particles with a diameter of 6 µm were added inside a mixture of olivine and pyroxene. For each meteorite, the best match between the modeled and the measured spectrum was obtained by utilizing different amounts of microiron scatterers inside a medium containing different ratios of olivine and pyroxene. All of the meteorite spectra were modeled at an absolute reflectance level without any normalizations.

The results show that by using only three different materials, our methods are capable of simulating meteorite spectra with good precision. However, the model used for this work was preliminary and multiple factors must be considered when

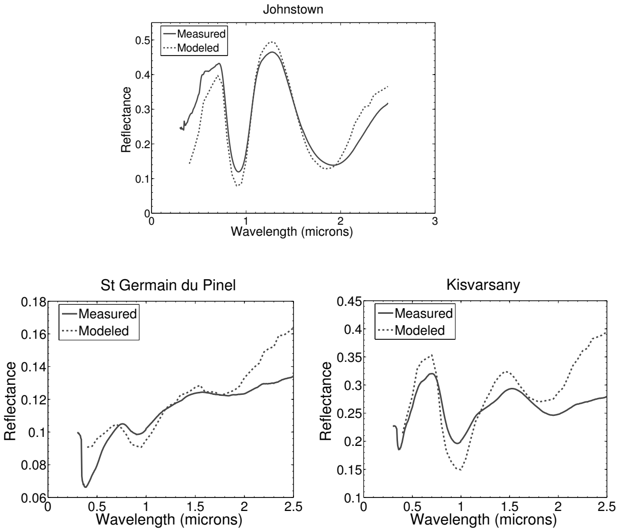

Figure 4.4: The modeled and measured absolute reflectance spectra of Kisvarsany, Johnstown, and St. Germain du Pinel meteorites.

studying the differences between the modeled and measured spectra. There are many types of olivines and pyroxenes, and the types that we used in our model could have been different in the meteorite sample. Furthermore, the meteorite surfaces were modeled as if they were powder. This causes an error in the absolute level of the spectrum as powders are generally brighter than flat, solid surfaces.

4.3 Asteroid (4) Vesta

As the Dawn space probe visited Vesta in 2011, it is a relatively well-known asteroid and a good candidate to test our light-scattering methods on. Furthermore, Vesta's surface is not significantly affected by space weathering and, thus, it can be omitted from the model. Below, I present the results and simulation framework for the spectroscopy, photometry, and polarimetry of (4) Vesta.

4.3.1 Spectroscopy, photometry, and polarimetry

In Paper IV, we modeled the absolute reflectance spectra of Vesta that were observed by Reddy (2011). The final dataset consisted of 12 spectra that were observed at a

17.4° phase angle. Using the prior knowledge that Vesta's surface regolith consists mostly of howardite, we needed to use one material in the simulations. The required complex refractive indices were derived using the optimization algorithm (see 4.1.2) and the measured reflectance spectrum of howardite powder.

The absolute spectral modeling was carried out for the wavelength region of 0.4 to 2.5 µm with 0.1 µm steps. As regolith grains have various shapes and sizes, we used the power-law distribution of GRS particles with different power-law indices to characterize different particle sizes. The computations were performed using SIRIS4 with GRS shapes for three size ranges: 10 to 50 µm, 10 to 100 µm, and 10 to 200 µm. Since the observed spectra were measured at a 17.4° phase angle, shadowing can affect the absolute level of the spectrum, and thus the final simulated spectra were studied at the same angle. The results show that the most realistic size range from 10 to 200 µm produces an excellent match with the observations when using a realistic power-law index 3.2. This suggests that Vesta's surface is dominated by small howardite particles which is consistent with previous studies (Hiroi et al., 1994). The small differences, mainly in longer wavelengths, between the modeled and observed spectra can be caused by, first, omitting resonance domain particles from the model, second, not accounting for temperature effects, third, using a wrong type of howardite or too few materials in the model, or fourth, using an incorrect particle size distribution.

To further analyse how much the shapes of the GRS can affect the model, we performed sensitivity tests on the derived m_{im} and the simulated spectra. The results show that the derived m_{im} did not vary significantly. However, the error caused by the shape on the simulated spectrum was 0.2 in the modeled reflectance.

In Paper VI, we completed the modeling work for Vesta by taking into account photometric and polarimetric observations at $\lambda = 0.45$ µm. The opposition effect seen in the observations is assumed to be caused by the wavelength-scale particles, and thus they needed to be added into the model and combined with the larger particles computed earlier. We performed the resonance domain computations using Voronoi particles in JVIE. The averaged scattering matrix of the large particles, and the amplitude matrix of the wavelength-scale particles were then used as input for RT-CB to retrieve the scattering properties of a surface that contained both small and large particles. The best match between the modeled values and the observations was obtained by assuming the fraction of the small-particle medium in the Vesta regolith to be 1%.

By taking into account wavelength-scale particles, we are able to produce the non-linear brightness surge and the negative degree of linear polarization at the backscattering direction seen in the observed photometric and polarimetric phase

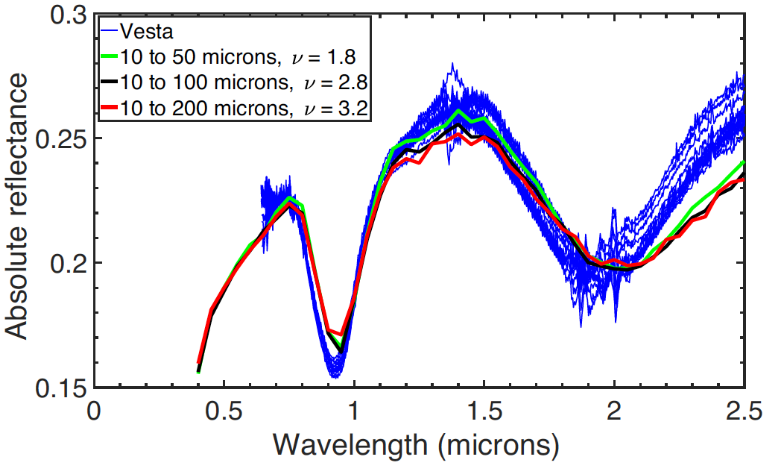

Figure 4.5: The modeled and measured absolute reflectance spectra of Vesta.

curves. At 0.45 µm, Vesta's geometric albedo value retrieved by our model is 0.32 which is in agreement with observations. However, the simulations were carried out for a single wavelength because there is no observational data for the whole wavelength region. Future studies should include several wavelengths to see the effect of the wavelength-scale particles on the whole spectrum.

In general, our study shows that modeling the asteroid regolith is challenging. Choosing the suitable particle shapes, size distributions, materials, and numerical methods is not straightforward, and typically there are multiple ways to model the surface. Additionally, space weathering plays a part on most asteroids, and needs to be accounted for (see, e.g. Penttilä et al., 2020).

4.4 Asteroid phase curve parameters from Gaia data

Asteroid phase curve parameters are related to the physical properties of the asteroid's surface, and thus can be extremely useful when studying taxonomic classification (Shevchenko et al., 2016; Penttilä et al., 2016). Here, I present lightcurve inversion on photometric data from Gaia Data Release 2 (Gaia DR2; Gaia Collaboration et al., 2018a; Gaia Collaboration et al., 2018b) and ground-based photometry (Durech et al., 2010) from Database of Asteroid Models from Inversion Techniques

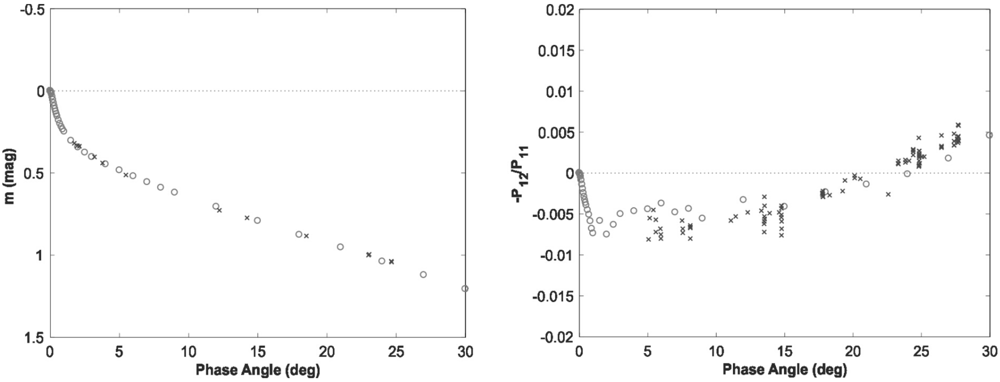

Figure 4.6: The modeled (red dots) and observed (blue crosses) photometry and polarimetry of Vesta.

(DAMIT). The work was carried out in Paper VII, where the methods and results are presented in detail.

4.4.1 Observational data

Our data set contained photometric observations from Gaia DR2 and DAMIT. The Gaia DR2 consists of astrometric and photometric data for about 14000 Solar System objects, a vast majority of them being asteroids (Cellino et al., 2019). As the photometric data has milli-magnitude precision, it is valuable when used to derive information on the asteroid's physical properties. The Gaia data was complemented with ground-based observations from the DAMIT database. DAMIT is constantly updated and provides the shape model, the sidereal rotation period, the spin axis direction, and the photometric data used for the inversion for more than three thousand asteroids.

4.4.2 Lightcurve inversion

We performed lightcurve inversion for 491 asteroids using the LCI-algorithm described in Chapter 3. The intersection of DAMIT and Gaia DR2 contains 2479 asteroids. The asteroids were selected so that there were at least six Gaia observations and at least two lightcurves for each target. We required at least three different phase angles for each asteroid, furthermore, the absolute rms values for the least-squares solutions of the Gaia data should be smaller than or equal to 0.015 mag and the absolute residual values smaller or equal to 0.025 mag. We excluded the Lowell

Observatory data (Oszkiewicz et al., 2011) because it has large uncertainties and the observations were carried out without a filter. The changes in the slope are so subtle that we wanted to make sure that no further uncertainties are introduced by different bands or filters.

Lightcurve inversion using both ellipsoid and convex shapes was applied to a collection of data that contained the sparse photometric Gaia observations and the ground-based observations from DAMIT. The initial rotation period, ecliptic pole longitude, and ecliptic pole latitude were retrieved from DAMIT, and the initial slope parameter β_{S} was set to 1.75 mag/rad as it is in the borderline of the slope values for multiple different Tholen classes (Penttilä et al., 2016) and changing the value does not affect the results significantly.

The derived proper phase curve slopes β_{S} showed that convex shapes produce more realistic results than ellipsoid shapes. We then used convex shapes to compute lightcurve-brightness-maxima based slopes β_{max} and mean-magnitude reference slopes β_{ref} (see Paper VII) to analyse the assumed taxonomic classes. Our analysis indicated that some of the asteroids do not sit well in their current taxonomic class, and a re-classification should be considered. Furthermore, the derived rotation periods and pole orientations showed that the model parameters of a few asteroids in the DAMIT database could be improved.

To extend our analysis, we retrieved absolute magnitudes for 345 asteroids and photometric phase curves with the H, G_1, G_2 fits for 312 asteroids. The computed absolute magnitudes were compared with the absolute magnitudes retrieved from the Jet Propulsion Laboratory (JPL) Small-Body Database. The differences between the values were fairly small but expected since we derived our magnitudes in the Gaia G band, whereas the JPL magnitudes were obtained in the V band. Finally, we compared the derived G_1 and G_2 parameters with the maxima-based G_1 and G_2 parameters for different Tholen classes (see Fig. 4.7). The results suggest that two groups can be distinguished: the first group contains M, S, and D types with moderate albedos, the second group contains P, C, X, G, and F types with low albedos. The A, E, T, B, and Q types each had only one target. The E-type high albedo asteroid and the T-type asteroid can be grouped together with the first group, whereas the B-type asteroid belongs to the second group. The A-type and the Q-type asteroids do not belong to any group, however, as each of them represents a single asteroid, the uncertainties can be large.

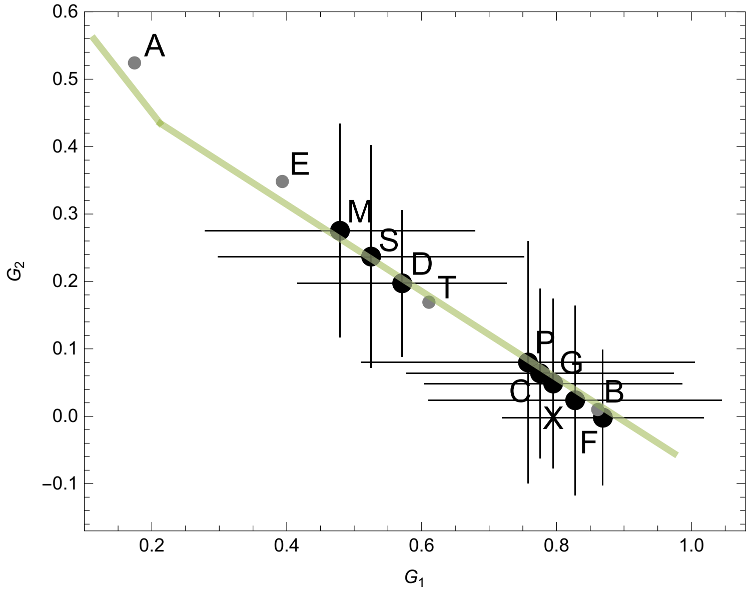

Figure 4.7: The distributions of the different Tholen classes (black dots) and their uncertainties (black crosses) in the G_1 and G_2 parameter space based on the reference phase curves. The green line shows how the G_{12} parameter maps into G_1 and G_2 in the H,G_{12} magnitude system and the grey dots represent single asteroids.

5 Summary of the publications

The thesis consists of seven refereed journal publications.

- **Paper I:** Penttilä A., Martikainen J., Gritsevich M., Muinonen K., (2018), Laboratory spectroscopy of meteorite samples at UV-vis-NIR wavelengths: Analysis and discrimination by principal components analysis, *Journal of Quantitative Spectroscopy and Radiative Transfer*, 206:189–197.
- **Paper II:** Lindqvist H., Martikainen J., Räbinä J., Penttilä A., Muinonen K., (2018), Ray optics for absorbing particles with application to ice crystals at near-infrared wavelengths, *Journal of Quantitative Spectroscopy and Radiative Transfer*, 217:329–337.
- **Paper III:** Martikainen J., Penttilä A., Gritsevich M., Lindqvist H., Muinonen K., (2018), Spectral modeling of meteorites at UV-vis-NIR wavelengths , *Journal of Quantitative Spectroscopy and Radiative Transfer*, 204:144–151.
- **Paper IV:** Martikainen J., Penttilä A., Gritsevich M., Videen G., Muinonen K., (2019), Absolute spectral modelling of asteroid (4) Vesta, *Monthly Notices of the Royal Astronomical Society*, 483:1952–1956.
- **Paper V:** Väisänen T., Martikainen J., Muinonen K., (2020), Scattering of light by dense particulate media in the geometric optics regime, *Journal of Quantitative Spectroscopy and Radiative Transfer*, 241.
- **Paper VI:** Muinonen K., Väisänen T., Martikainen J., Markkanen J., Penttilä A., Gritsevich M., Peltoniemi J., Blum J., Herranen J., Videen G., Maconi G., Helander P., Salmi A., Kassamakov I., Haeggström E., (2019), Scattering and absorption of light in planetary regoliths, *Journal of Visual Experiments*, 149.
- **Paper VII:** Martikainen J., Muinonen K., Penttilä A., Cellino A., Wang X.-B., (2020), Asteroid absolute magnitudes and phase curve parameters from Gaia photometry, *Astronomy & Astrophysics*, submitted

5.1 Paper I

Spectroscopic measurements of 30 meteorite samples were carried out using the University of Helsinki integrating-sphere UV-Vis-NIR spectrometer. Our data was further complemented with 14 spectra from the Planetary Data System (PDS) meteorite spectra database. We perform principal component analysis (PCA) on the measured reflectance spectra in order to identify features from the spectra that group similar targets together. The analysis shows that ordinary chondrites can be grouped together, and HED meteorites, aubrites, and enstatites can be separated. However, we are not able to separate H, L, and LL types of ordinary chondrites from each other.

The research was coordinated together with A. Penttilä. The author of this thesis carried out the spectral measurements of the 30 meteorite samples, and wrote significant parts of the manuscript.

5.2 Paper II

In this study, we implement corrections for inhomogeneous waves into the SIRIS-code. The new SIRIS4 is applied to ice crystals at near-infrared wavelengths using both hexagonal and GRS shapes, and further compared with traditional ray optics (SIRIS3) and discrete exterior calculus (DEC) that gives the exact result. We notice that the single-scattering albedo computed with SIRIS4 increases systematically throughout the NIR spectrum for both of the shapes. The comparisons between SIRIS3 and SIRIS4 against the DEC show that the ray-optics solution that accounts for the inhomogeneous waves is generally closer to the exact solution.

The research was coordinated together with H. Lindqvist and K. Muinonen. The author implemented GRS particles into the SIRIS4-code, and carried out all the SIRIS3 and SIRIS4 computations for the GRS shapes. The author also contributed in the writing of the manuscript.

5.3 Paper III

In this paper, we use SIRIS4 to model the reflectance spectra of Kisvarsany, Johnstown, and St. Germain du Pinel meteorites. For the modeling, we need the complex refractive indices of olivine, pyroxene, and iron. First, we retrieve the imaginary part of the complex refractive indices $m_{\rm im}$ of clinopyroxene by utilizing an optimization code that uses the measured reflectance spectra of the material and SIRIS4 with GRS shapes. We show that the derived $m_{\rm im}$ produces realistic spectra when using different grain sizes. After showing that our method works, we derive the $m_{\rm im}$ values of bronzite, which is then used in our model together with olivine and iron. Finally, we study how the shapes of the GRS particles affect the resulting spectra. We find that using only olivine, pyroxene, and iron, the meteorite spectra can be simulated with reasonable accuracy.

The author wrote the manuscript, implemented diffuse scatterers into SIRIS4, wrote the optimization code to retrieve refractive indices, as well as carried out all the computations and GRS sensitivity analyses.

5.4 Paper IV

Here we model the absolute reflectance spectrum of asteroid (4) Vesta using SIRIS4. We derive the m_{im} for howardite powder measured by T. Kohout, and use it to model Vesta's surface regolith and its particle size distribution. We simulate three different particle size ranges 10-50 µm, 10-100 µm, and 10-200 µm using power-law distribution with different power-law indices. Vesta's observed spectrum was obtained by Reddy (2011) at a 17.4° phase angle, therefore, the modeled spectrum is studied at the same angle. We choose the particle size range from 10 to 200 µm as it is the most realistic one, and find that the power-law distribution with index 3.2 produces a good match between the modeled and observed Vesta spectra. To conclude the study, we analyse how the shapes of the GRS particles affect the derived m_{im} and modeled spectrum. The results show that, in the case of the derived m_{im}, the shape did not have a significant impact, however, in the case of the modeled spectrum, the error caused by the shape was 0.2.

In this paper, the author was responsible for writing the manuscript and carried out all the computations and tests. The research was planned together with K. Muinonen and A. Penttilä.

5.5 Paper V

This paper studies light scattering by dense particulate media in the geometric optics region. We utilize a SIRIS framework with arbitrary meshes to compute light scattering by particulate media that consist of different materials, and compare the results with those obtained using the classical RT approach. Additionally, we introduce a hybrid diffuse geometric optics method that uses extinction distance distributions instead of a single value for the extinction mean free path. The hybrid model consists of a diffusely scattering core and a mantle made of discrete particles. The computations show that RT does not work if the medium is dense with complex size distributions. The hybrid model produces the best match when compared to a solution that is obtained by using a pure geometric optics ray tracing.

The author computed the extinction mean free paths together with T. Väisänen, and took part in the writing of the manuscript. T. Väisänen computed the results, and implemented a new SIRIS framework that supports arbitrary meshes with various materials.

5.6 Paper VI

This paper is a video article that demonstrates light scattering in planetary regoliths. The article is divided into theoretical, experimental, and numerical methods. The experimental part introduces acoustic levitation of samples for non-contact, non-destructive scattering measurements. The numerical methods focus on modeling the scattering media for various Solar System objects. The most relevant part for this thesis is the photometric and polarimetric study of asteroid (4) Vesta that completes the work started in Paper IV. The resonance-domain howardite particles are modeled using Voronoi shapes in JVIE, whereas the geometric optics region is simulated using SIRIS4 with GRS particles. The scattering properties of a surface containing both small and large particles are obtained by taking the averaged scattering matrix computed with SIRIS4, and the amplitude scattering matrix computed with JVIE, and using them as input for RT-CB. We find that the resulting photometric and polarimetric phase curves match well with the observations at the modeled wavelength.

This research was a collaboration of several people coordinated by K. Muinonen. The spectroscopic, photometric, and polarimetric modeling of (4) Vesta was completely carried out by the author. The author wrote the parts of the manuscript that deal with the modeling of Vesta's surface.

5.7 Paper VII

In this paper, we performed lightcurve inversion for 491 asteroids using triaxial ellipsoid and convex shapes. The data set contained photometric observations from Gaia DR2 and DAMIT. For each asteroid, we derived photometric slope parameters, rotation periods, and pole orientations. Furthermore, we retrieved absolute magnitudes, and mean-magnitude reference phase curve slopes in the G band for 345 asteroids. The retrieved slope parameters were used to study the taxonomic classification of the selected asteroids, and the absolute magnitudes were compared with those obtained from the Jet Propulsion Laboratory Small-Body Database. Finally, the derived reference phase curves were fitted with the H,G_1,G_2 phase function for 312 asteroids, and the resulting G_1,G_2 distribution was compared with the G_1,G_2 dependence based on the lightcurve-brightness-maxima photometry.

This research was planned together with K. Muinonen and A. Penttilä. The author carried out all the convex and ellipsoid retrievals for each asteroid, as well as computed the absolute magnitudes. K. Muinonen provided the LCI-algorithm as well as the algorithm to compute the absolute magnitudes. The author wrote an algorithm to apply the methods to all asteroids. Data analysis was carried out together with K. Muinonen and A. Penttilä. A. Penttilä applied the H,G_1,G_2 phase function fit to the derived reference phase curves.

6 Concluding remarks

The thesis can be divided into two parts: development of the light-scattering methods and modeling planetary surfaces. Papers II and V focus on the methods, whereas Papers I, III, IV, VI, and VII are based on numerical simulations and laboratory measurements.

Numerical simulations reveal that modeling planetary surfaces is not simple, as the outcome depends on multiple variables, such as the particle shapes and sizes, materials, packing densities, and the selected methods. Each model is case-dependent, and choosing the most suitable materials and methods can be challenging. Furthermore, most numerical methods require complex refractive indices of the materials that are usually not easily available, which is why we developed an optimization algorithm (Paper III) to derive complex refractive indices from laboratory measurements. This is an important application, as it can be used widely in different studies.

In Paper III, we study a simplified scenario where the meteorite surfaces consist of a mixture of up to three different materials. The model is capable of producing realistic absolute spectra but it is evident that the model was not complete and needed more work. In Paper IV, we develop our simulation framework further by modeling the surface regolith of asteroid (4) Vesta using howardite. The reflectance spectrum is simulated with GRS particles larger than the wavelength with a power-law size distribution. The model provides a good match when compared to the spectroscopic observations, however, photometric and polarimetric observations cannot be explained without including wavelength-scale particles in the simulations. In Paper VI, we upgrade the model by accounting for the resonance domain with Voronoi-shaped particles. The simulated photometric and polarimetric phase curves show good results as they match the observations almost perfectly. Furthermore, the derived geometric albedo is in agreement with the observed value. It is important to note that the complete model utilized a single wavelength because we lack photometric and polarimetric observations. In the future, it is crucial to obtain more photometric and polarimetric data at several wavelengths to study how the wavelength-scale particles affect the whole spectrum.

The thesis is completed in Paper VII, where we derive photometric slopes, rotation periods, and pole orientations for 491 asteroids using photometric data from Gaia DR2 and DAMIT. Furthermore, we retrieve G-band absolute magnitudes and mean-magnitude reference phase curves for 345 asteroids. As the photometric slope relates to the physical properties of the asteroid's surface, it can be used in taxonomic classification to complement spectroscopic data. Our analysis reveals that the taxonomic classes should be revised for at least a few of the asteroids. Future studies should include a wider selection of asteroids to investigate the possible misclassifications by the current classification systems.

To conclude, the simulation frameworks introduced in this thesis provide a way to understand the compositions of the asteroid surfaces. Most of the methods are applicable to other Solar System objects, such as comets (see Paper VI). Ongoing and future space missions will provide us more data to study, and our methods will play a vital role in interpreting the observations.

Bibliography

Bohren, C. F. and Huffman, D. R. (1983). *Absorption and scattering of light by small particles.* New York: Wiley, 1983.

Bus, S. J. and Binzel, R. P. (2002). Phase II of the Small Main-Belt Asteroid Spectroscopic Survey. A Feature-Based Taxonomy. *Icarus*, 158(1):146–177.

Cellino, A., Hestroffer, D., Lu, X. P., Muinonen, K., and Tanga, P. (2019). Inversion of HIPPARCOS and Gaia photometric data for asteroids. Asteroid rotational properties from sparse photometric data. *Astronomy & Astrophysics*, 631:A67.

Chang, P. C., Walker, J., and Hopcraft, K. (2005). Ray tracing in absorbing media. *Journal of Quantitative Spectroscopy and Radiative Transfer*, 96(3):327–341.

Clark, B. E., Hapke, B., Pieters, C., and Britt, D. (2002). Asteroid space weathering and regolith evolution. In Bottke, Jr., W. F., Cellino, A., Paolicchi, P., and Binzel, R. P., editors, *Asteroids III*, pages 585–599. University of Arizona Press, Tucson.

Clayton, R. N. and Mayeda, T. K. (1989). Oxygen Isotope Classification of Carbonaceous Chondrites. In *Lunar and Planetary Science Conference*, volume 20 of *Lunar and Planetary Science Conference*, page 169.

DeMeo, F. E., Binzel, R. P., Slivan, S. M., and Bus, S. J. (2009). An extension of the Bus asteroid taxonomy into the near-infrared. *Icarus*, 202(1):160–180.

Dupertuis, M. A., Proctor, M., and Acklin, B. (1994). Generalization of complex Snell–Descartes and Fresnel laws. *Journal of the Optical Society of America A*, 11(3):1159–1166.

Durech, J., Sidorin, V., and Kaasalainen, M. (2010). DAMIT: a database of asteroid models. *Astronomy & Astrophysics*, 513:A46.

Egel, A., Pattelli, L., Mazzamuto, G., Wiersma, D. S., and Lemmer, U. (2017). Celes: Cuda-accelerated simulation of electromagnetic scattering by large ensembles of spheres. *Journal of Quantitative Spectroscopy and Radiative Transfer*, 199:103–110.

Epstein, P. S. (1930). Geometrical optics in absorbing media. *Proceedings of the National Academy of Sciences*, 16(1):37–45.

Gaia Collaboration, Spoto, F., Tanga, P., Mignard, F., Berthier, J., Carry, B., Cellino, A., Dell'Oro, A., Hestroffer, D., Muinonen, K., Pauwels, T., Petit, J., David, P., De Angeli, F., Delbo, M., Frezouls, B., Galluccio, L., Granvik, M., Guiraud, J., Hernandez, J., Ordenovic, C., Portell, J., Poujoulet, E., Thuillot, W., Walmsley, G., Brown, A., Vallenari, A., Prusti, T., de Bruijne, J., Babusiaux, C., Bailer-Jones, C., Biermann, M., Evans, D., Eyer, L., Jansen, F., Jordi, C., Klioner, S., Lammers, U., Lindegren, L., Luri, X., Panem, C., Pourbaix, D., Randich, S., Sartoretti, P., Siddiqui, H., Soubiran, C., van Leeuwen, F., Walton, N., Eriksson, K., Fedorets, G., and Siltala, L. (2018a). Gaia data release 2 observations of solar system objects. *Astronomy & Astrophysics*, 616.

Gaia Collaboration, Brown, A. G. A., et al. (2018b). Gaia Data Release 2. Summary of the contents and survey properties. *Astronomy & Astrophysics*, 616:A1.

Gehrels, T., Coffeen, T., and Owings, D. (1964). Wavelength dependance of polarization. III. The lunar surface. *The Astronomical Journal*, 69:826.

Griffiths, D. J. (2013). *Introduction to electrodynamics; 4th ed.* Pearson, Boston, MA. Re-published by Cambridge University Press in 2017.

Hapke, B. (2008). Bidirectional reflectance spectroscopy: 6. effects of porosity. *Icarus*, 195:918–926.

Hapke, B. W. (1963). A theoretical photometric function for the lunar surface. *Journal of Geophysical Research*, 68:4571–4586.

Harris, A. and Lupishko, D. (1989). Photometric lightcurve observations and reduction techniques. *Asteroids II.*

Hiroi, T., Pieters, C. M., and Takeda, H. (1994). Grain Size of the Surface Regolith Asteroid 4 Vesta Estimated from Its Reflectance Spectrum in Comparison with HED Meteorites. *Meteoritics*, 29(3):394.

Kaasalainen, M., Lamberg, L., and Lumme, K. (1992). Interpretation of lightcurves of atmosphereless bodies. II - Practical aspects of inversion. *Astronomy & Astrophysics*, 259(1):333–340.

Kohout, T., Čuda, J., Filip, J., Britt, D., Bradley, T., Tuček, J., Skála, R., Kletetschka, G., Kašlík, J., Malina, O., Šišková, K., and Zbořil, R. (2014). Space weathering simulations through controlled growth of iron nanoparticles on olivine. *Icarus*, 237:75–83.

Lamberg, L. (1993). *Vol. 315L.* PhD thesis, University of Helsinki, Finland.

Lindqvist, H., Martikainen, J., Räbinä, J., Penttilä, A., and Muinonen, K. (2018). Ray optics for absorbing particles with application to ice crystals at near-infrared wavelengths. *Journal of Quantitative Spectroscopy & Radiative Transfer*, 217:329–337.

Markkanen, J., Yla-Oijala, P., and Sihvola, A. (2012). Discretization of volume integral equation formulations for extremely anisotropic materials. *IEEE Transactions on Antennas and Propagation*, 60(11):5195–5202.

Markkanen, J., Penttilä, A., Peltoniemi, J., and Muinonen, K. (2015). Inhomogeneous particle model for light-scattering by cometary dust. *Planetary and Space Science*, 118:164–172. SI:ACM Interrelated.

Martikainen, J., Penttilä, A., Gritsevich, M., Lindqvist, H., and Muinonen, K. (2018). Spectral modeling of meteorites at uv-vis-nir wavelengths. *Journal of Quantitative Spectroscopy & Radiative Transfer*, 204:144–151.

Martikainen, J., Muinonen, K., Penttilä, P., Cellino, A., and Wang, X.-B. (2020). Asteroid absolute magnitudes and phase curve parameters from Gaia photometry. *Astronomy & Astrophysics*, Submitted.

McSween, H. Y., Binzel, R. P., de Sanctis, M. C., Ammannito, E., Prettyman, T. H., Beck, A. W., Reddy, V., Corre, L., Gaffey, M. J., McCord, T. B., Raymond, C. A., and Russell, C. T. (2013). Dawn; the Vesta-HED connection; and the geologic context for eucrites, diogenites, and howardites. *Meteoritics and Planetary Science*, 48(11):2090–2104.

Mishchenko, M., Travis, L., and Lacis, A. (2006). *Multiple Scattering of Light by Particles: Radiative Transfer and Coherent Backscattering.* Cambridge University Press.

Muinonen, K. (1990). *Light scattering by inhomogeneous media: backward enhancement and reversal of linear polarization.* Observatory and Astrophysics Laboratory, University of Helsinki, Finland.

Muinonen, K., Nousiainen, T., Fast, P., Lumme, K., and Peltoniemi, J. (1996). Light scattering by Gaussian random particles: Ray optics approximation. *Journal of Quantitative Spectroscopy and Radiative Transfer*, 55(5):577–601.

Muinonen, K. (2004). Coherent backscattering of light by complex random media of spherical scatterers: numerical solution. *Waves in Random Media*, 14(3):365–388.

Muinonen, K., Nousiainen, T., Lindqvist, H., Muñoz, O., and Videen, G. (2009). Light scattering by Gaussian particles with internal inclusions and roughened surfaces using ray optics. *Journal of Quantitative Spectroscopy and Radiative Transfer*, 110(14):1628–1639.

Muinonen, K., Belskaya, I. N., Cellino, A., Delbò, M., Levasseur-Regourd, A.-C., Penttilä, A., and Tedesco, E. F. (2010). A three-parameter magnitude phase function for asteroids. *Icarus*, 209(2):542–555.

Muinonen, K., Parviainen, H., Näränen, J., Josset, J.-L., Beauvivre, S., and Pinet, P. (2011). Lunar surface properties with SMART-1 AMIE. *Astronomy & Astrophysics*, 531.

Muinonen, K., Torppa, J., Wang, X. B., Cellino, A., and Penttilä, A. (2020). Asteroid lightcurve inversion with Bayesian inference. *Astronomy & Astrophysics*, 642:A138.

Oszkiewicz, D., Muinonen, K., Bowell, E., Trilling, D., Penttilä, A., Pieniluoma, T., Wasserman, L., and Enga, M.-T. (2011). Online multi-parameter phase-curve fitting and application to a large corpus of asteroid photometric data. *Journal of Quantitative Spectroscopy & Radiative Transfer*, 112:1919–1929.

Penttilä, A., Lumme, K., Hadamcik, E., and Levasseur-Regourd, A. C. (2005). Statistical analysis of asteroidal and cometary polarization phase curves. *Astronomy & Astrophysics*, 432(3):1081–1090.

Penttilä, A., Shevchenko, V. G., Wilkman, O., and Muinonen, K. (2016). H, G_1, G_2 photometric phase function extended to low-accuracy data. *Planetary and Space Science*, 123:117–125.

Penttilä, A., Väisänen, T., Markkanen, J., Martikainen, J., Kohout, T., Videen, G., and Muinonen, K. (2020). Rigorous light-scattering simulations of nanophase iron space-weathering effects on reflectance spectra of olivine grains. *Icarus*, 345.

Reddy, V. (2011). Vesta Rotationally Resolved Near-Infrared Spectra V1.0. *NASA Planetary Data System*, pages EAR–A–I0046–3–REDDYVESTA–V1.0.

Shepard, M. K. and Helfenstein, P. (2007). A test of the Hapke photometric model. *Journal of Geophysical Research (Planets)*, 112(E3):E03001.

Shevchenko, V. G., Belskaya, I. N., Muinonen, K., Penttilä, A., Krugly, Y. N., Velichko, F. P., Chiorny, V. G., Slyusarev, I. G., Gaftonyuk, N. M., and Tereschenko, I. A. (2016). Asteroid observations at low phase angles. IV. Average parameters for the new H, G_1, G_2 magnitude system. *Planetary and Space Science*, 123:101–116.

Shkuratov, I. G. (1988). A diffraction mechanism for the formation of the opposition effect of the brightness of surfaces having a complex structure. *Kinematika i Fizika Nebesnykh Tel*, 4:33–39.

Shkuratov, Y., Ovcharenko, A., Zubko, E., Miloslavskaya, O., Muinonen, K., Piironen, J., Nelson, R., Smythe, W., Rosenbush, V., and Helfenstein, P. (2002). The opposition effect and negative polarization of structural analogs for planetary regoliths. *Icarus*, 159(2):396–416.

Simonelli, D. P., Veverka, J., Thomas, P. C., Helfenstein, P., Carcich, B. T., and Belton, M. J. S. (1996). Ida Lightcurves: Consistency with Galileo Shape and Photometric Models. *Icarus*, 120(1):38–47.

Stankevich, D. G. and Shkuratov, Y. G. (2002). Multiple Scattering of Light in Regolith-like Media: Geometric Optics Approximation. *Solar System Research*, 36(5):409–416.

Tang, H., Wang, S., and Li, X. (2012). Simulation of nanophase iron production in lunar space weathering. *Planetary and Space Science*, 60(1):322–327.

Tholen, D. J. (1989). Asteroid taxonomic classifications. In Binzel, R. P., Gehrels, T., and Matthews, M. S., editors, *Asteroids II*, pages 1139–1150.

Väisänen, T., Martikainen, J., and Muinonen, K. (2020). Scattering of light by dense particulate media in the geometric optics regime. *Journal of Quantitative Spectroscopy & Radiative Transfer*, 241.

Waterman, P. C. (1965). Matrix formulation of electromagnetic scattering. *Proceedings of the IEEE*, 53(8):805–812.

Weisberg, M. K., Prinz, M., Clayton, R. N., Mayeda, T. K., Grady, M. M., Franchi, I., Pillinger, C. T., and Kallemeyn, G. W. (1996). The K (Kakangari) chondrite grouplet. *Geochimica Cosmochimica Acta*, 60(21):4253–4263.

Zubko, E., Kimura, H., Shkuratov, Y., Muinonen, K., Yamamoto, T., Okamoto, H., and Videen, G. (2009). Effect of absorption on light scattering by agglomerated debris particles. *Journal of Quantitative Spectroscopy and Radiative Transfer*, 110(14):1741–1749. XI Conference on Electromagnetic and Light Scattering by Non-Spherical Particles: 2008.